Super-resolution of Mammograms

Jun Zheng, Olac Fuentes, and Ming-Ying Leung

***Abstract*—High-quality mammography is the most effective technology presently available for breast cancer screening. High resolution mammograms usually lead to more accurate diagnoses; however, they require large doses of radiation, which may have harmful effects. In this paper, we present a method to synthesize high-resolution mammograms from low-resolution inputs, which offers the potential of allowing accurate diagnoses while minimizing risks to patients. Our algorithm combines statistical machine learning methods and stochastic search to learn the mapping from low-resolution to high-resolution mammograms using a large dataset of training image pairs. Experimental results show that the super-resolution algorithm can generate high-quality, high-resolution breast mammograms from low-resolution input with no human intervention.**

I. Introduction

Breast cancer causes more deaths than any other type of cancer for females worldwide. However, if breast cancer can be detected early, the five-year survival rate increases considerably [1]. High-quality mammography, which consists of using X-rays to examine the human breast, is the most effective technology presently available for breast cancer screening.

The quality of diagnoses depends on the resolution of the mammograms, among other factors, with higher resolutions providing a higher level of detail that normally leads to improved accuracy. However, to obtain higher resolutions, larger doses of radiation are necessary, which may have harmful effects for patients. To alleviate this problem, some work has been done attempting to increase the resolution of mammograms without a corresponding increase in radiation. Robinson et al. [2] used multi-frame image reconstruction to produce high-resolution mammograms beyond the native resolution of a digital image sensor by way of accurate sub-pixel registration of aliased images. Several other image enhancement techniques have been proposed for this problem [3], [4], [5], [6], [7], [8]; however, improvements have been modest.

Recent research at the intersection of computer vision and computer graphics has produced methods for automatically increasing the resolution of images of specific classes, commonly faces [9], [10]. These methods use statistical machine learning techniques to learn the function that maps low resolution images to their high resolution counterparts, for a particular class of images. Efforts to date in this line of work have focused on face images; one of the goals of this work is to investigate whether these methods can be extended to other domains, particularly medical image processing.

Jun Zheng and Olac Fuentes are with the Department of Computer Science, The University of Texas at El Paso, El Paso, TX, U.S.A., Ming-Ying Leung is with the Department of Mathematical Sciences and the Bioinformatics Program, The University of Texas at El Paso, El Paso, TX, U.S.A. (email: jzheng@miners.utep.edu, {ofuentes, mleung}@utep.edu).

This work was supported in part by NIH Grants NO. 2506GM008012-39 and 2G12RR008124-16A1

In this paper, we present an end-to-end method to synthesize a high-resolution (HR) mammogram given a low-resolution (LR) one as input. Our method receives as input low-resolution mammograms, which can be generated with low doses of X-ray radiation. Then these images are automatically registered and aligned using a mesh warping algorithm. Finally, a two-step super-resolution algorithm is applied, which integrates a PCA-based global model and a patch-based local model, to generate the high-resolution images. The experimental results show that the algorithm can generate high-quality high-resolution breast mammograms from low-resolution input with no manual registration.

II. Related Work

Existing methods for image super-resolution can be divided into two categories: multiple-frame super-resolution and single-frame super-resolution. In multiple-frame super-resolution, the LR frames typically depict the same scene. This means that LR frames are distorted as well as shifted with subpixel precision. If the LR frames contain different subpixel shifts, then the new information contained in each LR frame can be used to construct an HR frame. Through motion analysis from frame to frame, a super-resolution image can be inferred by combining these LR frames with subpixel accuracy [11].

Single-frame super-resolution aims to estimate missing high-resolution details from a single input low-resolution image. The problems under this category can be generic or object-specific. Generic image super-resolution techniques, such as interpolation, band-pass filtering, unsharp masking, and several others, can be applied to any images. However, they usually result in blurring of sharp edges, introduction of blocking artifacts, inability to generate high frequency components or fine details of semantically important structures [12], [13], [14], [15].

Object-specific super-resolution assumes that only images of a certain type are input. Most approaches to object-specific super-resolution use machine learning algorithms to find the function that maps low-resolution to high-resolution images of a given class. This enables them to infer the most likely high-resolution image depicting the same object as a low-resolution image given as input. When applied to face images, this process is known as face hallucination, first proposed by Baker and Kanade [16], [9], and has been an active research area for the last decade [17], [18], [14], [19], [20], [21], [10], [22].

Because of the benefits of image super-resolution, several methods have also been proposed for the purpose of medical image super-resolution. Irani et al. [3] proposed an iterative algorithm together with a method for image registration with subpixel accuracy to increase image resolution. The approach is similar to reconstruction of a 2-D object from its 1-D projections in computer aided tomography (CAT). Images are reconstructed from their projections in many directions in tomography, while in super-resolution, each low-resolution pixel is a projection of a region in the scene whose size is determined by the imaging blur. The high-resolution image is then constructed using an approach similar to the back-projection method used in CAT.

Based on Irani's work, Greenspan et al. [4] applied the iterative super-resolution algorithm to construct high-resolution magnetic resonance images (MRI). MRI slice thickness is determined by hardware limitations and pulse sequence timing considerations. Thus the in-plane resolution is higher than the resolution of the slice-select direction. They addressed the challenge of achieving HR isotropic 3-D MRI images by merging several sets of 2-D slices in slice-select direction.

Kennedy et al. [5], [6] successfully applied Irani's iterative super-resolution algorithm to construct positron emission tomographies (PET). PET resolution is limited by physical parameters such as scatter, counting statistics, positron range and patient motion, detector array geometry, and the implemented acquisition protocol. They demonstrated how an iterative super-resolution algorithm can be implemented to improve PET resolution using shifts and rotations in the transaxial plane as well as along the axial direction.

Hsu et al. [23] proposed a wavelet-based projection-onto-convex-set super-resolution reconstruction algorithm to enhance spatial resolution of MRI heart images from a temporal sequence. This approach makes use of the non-stationary effect in the successive images in the sequence to extract information for image reconstruction at a higher spatial resolution.

Lettington and Hong [24] proposed an efficient algorithm to reduce the ringing artifacts that arise from the use of the unconstrained Poisson maximum a posteriori (MAP). They use a Lorentzian probability function to model the image by studying the distribution of its edge values, then introduced a correction term to increase the image likelihood using mean square error (MSE) criterion. The correction term is effective in reducing the ringing artifacts while maintaining the sharpness of the image.

Kanemura et al. addressed the hyperparameter estimation problem in Bayesian image superresolution with a compound Gaussian Markov random field (MRF) prior [7]. They estimated all the hyperparameters, the registration parameters, and the HR image by means of minimizing variational free energy under the assumption of a factorized posterior.

Nguyen et al. [25] presented a new and efficient wavelet-based algorithm for image super-resolution that is a combination of interpolation and restoration processes and exploits the interlaced sampling structure in the low resolution data.

III. Super-resolution Algorithm

In this work we propose a mammogram super-resolution algorithm that can generate high-quality high-resolution images from low-resolution input with no manual registration. The proposed algorithm consists of four main steps. The first step automatically aligns the parts of the images containing the breasts to a standardized position. The second step uses eigentransformation to infer global models, that is, the low-frequency components of the target image. Principal Component Analysis (PCA) is used to fit the input images as a linear combination of the low resolution images in the training set. The HR images are then inferred by replacing the LR training images with HR ones, while retaining the same combination coefficients. In the third step, a patch-based one-pass algorithm captures high-frequency contents of the HR images. The fourth step re-maps the breasts back to their original position.

A. Automatic Alignment

Image alignment is a key step for the success of the algorithm. In practice, we cannot assume that any low-resolution mammogram has been accurately aligned, although the approximate position of the breasts is given by mammography sensors. Therefore, in preprocessing, we automatically align the breast cancer mammograms to make sure all breasts are in exactly the same position, and then do the super-resolution. The automatic alignment process consists of two parts, 2-pass mesh warping [26] and segmentation-based initialization.

The 2-pass mesh warping algorithm accepts a source image and two 2-D arrays of coordinates. The first array, S, specifies the coordinates of control points in the source image, and the second array, D, specifies their corresponding positions in the destination image. The first pass is responsible for resampling each row independently. It maps all (u, v) points to their (x, v) coordinates in the intermediate image I, in which the x-coordinates are the same as those in D, and y-coordinates are same as those in S.

For each pixel P in intermediate image I, the value of P is evaluated as a weighted sum from x_0 to x_1, the left most and rightmost positions in S that are the projections of the left and right integer-valued boundaries of P

$$P = \frac{\sum_{x=x_0}^{x_1} k_x S_x}{x_1 - x_0}$$

where k_x is the scale factor of source pixel S_x, and the subscript x denotes the index that lies between $\lfloor x_0 \rfloor$ and $\lceil x_1 \rceil$. The scale factor k_x is defined as

$$k_x = \begin{cases} \lceil x \rceil - x_0 & \text{if } \lfloor x \rfloor < x_0 \\ 1 & \text{if } x_0 \le x < x_1 \\ x_1 - \lfloor x \rfloor & \text{if } \lceil x \rceil > x_1 \end{cases}$$

The second pass then resamples each column in I, mapping every (x, v) point to its final (x, y) position, which is virtually identical to that of the first pass. We just need to substitute (x, v) for (u, v), and substitute (x, y) for (x, v) [26].

The key to apply 2-pass mesh warping is to build the 2-D arrays of coordinates. We use segmentation-based initialization

to build the 2-D arrays of coordinates automatically. The initialization for 2-pass mesh warping consists of the following steps (Figure 1):

1) Convert the input image to binary image.
2) Apply erosion to remove the labels in the binary image.
3) Convert the binary image to gradient image to find the edge.
4) Use skeletonization to reduce the edge to a single line.
5) Distribute points uniformly on each side of the line to generate mesh for 2-pass mesh warping.

B. Global Modeling

In global modeling we use an algorithm called eigentransformation, which was originally introduced by Wang and Tang [22]. The eigentransformation is a simple and powerful technique for image enhancement based on principal component analysis (PCA). It assumes that we have a training set of pairs of images $\langle (L_1, H_1), \ldots, (L_n, H_n) \rangle$, where each pair (L_i, H_i) contains a low resolution image L_i and its corresponding high-resolution counterpart H_i.

The eigentransformation allows any image L to be represented as a linear combination of images in the training set $L_1, ..., L_n$. When given a low resolution image, it finds the vector of coefficients $[c_1, \ldots, c_n]$ so that

$$L = \Sigma_{i=1}^{n} c_i L_i + \mu_L$$

where μ_L is the mean low-resolution image.

Given the vector $[c_1, \ldots, c_n]$, the approximate high resolution image H can be computed by

$$H = \Sigma_{i=1}^{n} c_i H_i + \mu_H$$

where μ_H is the mean high-resolution image.

Because the coefficients are not computed from the HR training data, some noise-like distortion may be introduced. To reduce the distortion, we apply constraints by bounding the projection onto each eigenvector by its corresponding eigenvalue, then the synthesized image is reconstructed from these constrained coefficients. The high resolution image obtained in this manner is called the *global model*, since it approximates the global properties of the target high-resolution image.

C. Local Modeling

Given a global model, to construct the corresponding local model, we first filter the global model with a Gaussian high-pass filter, and then subdivide the filtered global model into patches, which we call the low-frequency patches of the high-resolution (HR) images, by scanning a window across the image in raster-scan order. Similarly, we also filter and subdivide the HR images in the training set into patches that we call high-frequency patches of the training HR images.

To construct a local model, for each low-frequency patch, a high-frequency patch of the training HR image is selected by a nearest neighbor search from the training set based on local low-frequency details and adjacent HR patches previously determined. The selected high-frequency patch should not only come from a location in the training images that has a similar corresponding low-frequency appearance, but also agree with the overlapping pixels, which we call high-frequency overlap, at the edges of its previously determined high-frequency neighbors. This ensures that the high-frequency patches are compatible with those of the neighboring high-frequency patches.

In this work we compute the local model with an algorithm similar to Freeman's one-pass algorithm [18][14]. We first concatenate the pixels in the low-frequency patch and the high-frequency overlap to form a search vector. The training set also contains a set of such vectors. Then we search for a match by finding the nearest neighbor in the training set. When we find a match we extract the corresponding high-frequency patch from training data set and add it to the initial global model to obtain the output image.

Mathematically, this process can be described as follows. Suppose we have a training data set

$$\{(x^{(i,j,k)}, y^{(i,j,k)}, z^{(i,j,k)}),$$

$$i = 1, 2, \ldots, l; j = 1, 2, \ldots, m; k = 1, 2, \ldots, n\}$$

where $x^{(i,j,k)}$ is the low-frequency patch at the i^{th} row and j^{th} column of the k^{th} training HR image, $y^{(i,j,k)}$ is the corresponding high-frequency overlap and $z^{(i,j,k)}$ is the corresponding high-frequency patch of the training HR image, l is the number of rows of patches in a training image, m is the number of columns of patches in a training image and n is the number of training images.

Given an input LR patch $\overline{x}$, we need to find an HR patch $z^{(i',j',k')}$ such that

$$z^{(i',j',k')} = \min_{i,j,k}(d(\overline{x}, x^{(i,j,k)}) + \alpha * (d(y^{(i,j,k)}, y_N^{(i,j,k)})))$$

where $d(x, y)$ is the Euclidean distance between x and y, $y_N^{(i,j,k)}$ is the overlap of $z^{(i,j,k)}$ with the adjacent, previously determined high-frequency patches, which are the patches above and to the left of the current high-frequency patch in the local model, α is a user-controlled weighting factor, and $z^{(i',j',k')}$ is the selected high-frequency patch.

D. Image Quality Measures

In this paper, the quality of a super-resolution image is defined as the similarity with the original high-resolution image. We use Peak Signal-to-Noise Ratio ($PSNR$) and the Mean Structural Similarity ($MSSIM$) index to measure the quality of super-resolution results. Let X and Y be two images to be compared, and T be the total number of pixels in either image. The $PSNR$, which is most commonly used as a measure of quality of reconstruction [27], is defined as

$$PSNR = 20 \times log_{10} \frac{255}{RMSE}$$

where $RMSE$ is the root mean square error between the two images.

(a) (b) (c) (d) (e) (f)

Fig. 1. Automatic registration: (a) Original image. (b) Converting the original image to binary image. (c) Using erosion to remove the labels in the binary image. (d) Converting the binary image to gradient image to find the edge. (e) Using skeletonization to reduce the edge to a single line. (f) Sampling points on the line and making the mesh.

$$\begin{aligned} RMSE(X,Y) &= \sqrt{MSE(X,Y)} \\ &= \sqrt{E((X-Y)^2)} \\ &= \sqrt{\frac{\sum_{i=1}^{T}(x_i-y_i)^2}{T}} \end{aligned}$$

The structural similarity (SSIM) index [28] is an implementation of the idea of structural similarity, from an image formation point of view, which takes into account contrast, luminance, and structure to determine similarity between two images. $SSIM$ is defined as

$$SSIM(x,y) = \frac{(2\mu_x\mu_y + C1)(2\sigma_{xy} + C2)}{(\mu_x^2 + \mu_y^2 + C1)(\sigma_x^2 + \sigma_y^2 + C2)},$$

$$\sigma_{xy} = \frac{1}{T-1}\sum_{i=1}^{T}(x_i - \mu_x)(y_i - \mu_y)$$

where x and y are subimages of X and Y, μ_x is the average of x, μ_y is the average of y, σ_x is the standard deviation of x, σ_y is the standard deviation of y. $C1 = (k_1 L)^2$ and $C2 = (k_2 L)^2$ are two variables to stabilize the division with weak denominator, L is the dynamic range of the pixel values (typically this is 255), $k_1 = 0.01$ and $k_2 = 0.03$ by default. The mean SSIM (MSSIM) is then simply the mean of the SSIMs for each subimage. A value of MSSIM of 1 indicates perfect similarity [28].

IV. Experimental Results

We use DDSM (Digital Database for Screening Mammography) for our experiments. DDSM is a standard dataset used by the mammography image analysis research community. The database has about 2,500 cases. Each case includes two images of each breast, along with some associated patient information and image information.

In this work, 400 normal left mediolateral oblique (MLO) images from DDSM dataset are used for training and 10 normal left MLO images images for testing. And we use an automatically built 32×8 mesh to register the mammograms.

To construct our training dataset, we generate global models from the training LR mammograms and filter them with a Gaussian high-pass filter. Then we divide the filtered global model into low-frequency patches by scanning a 4×4 pixel window across the images in raster-scan order. Then we again filter and subdivide the training HR mammograms into 4×4 pixel high-frequency patches. At each step we also get a 9-pixel overlap of each high-frequency patch with the high-frequency patches above and to the left. Then we create our training vectors by concatenating the low-frequency patches and corresponding high-frequency overlaps. In practice, the size of low-frequency patches and high-frequency patches is not necessarily the same. The parameter α, which controls the trade-off between matching the low-frequency patches and finding the most compatible high-frequency patches, is set to 0.2, which gives good HR results in our experiments.

To reduce the effect of background to the quantitative evaluation of the super-resolution results, we applied a mask to each image (Figure 3) to get the region of interests (ROI). The mask is computed automatically using image an segmentation algorithm. At the same time we removed the labels from the background.

For each high-resolution image, we downsample it by a downsample factor of 2,4,8 and 16, and then enhance the low-resolution image to its original resolution. The experimental results of different resolutions are reported in figures 2 to 5. We also measure the quality of super-resolution results using PSNR and MSSIM (Table I), which are commonly used image quality measures in most super-resolution studies [27]. The results indicate that the super-resolution images have much more high-frequency information than nearest and bilinear interpolated images.

Comparing the different image quality measures, we can see that although the PSNR is a meaningful standard image quality measure [27], it does not necessarily reflect perceived visual quality by humans [29][28]. In some of the experiments shown in Table I, the PSNR value of SR by a downsample factor of 4 is 34.02, which is lower than the corresponding PSNR value of bilinear interpolation, 35.2363. But from Figure 3, we can see that the SR results have much more detail information than the results of bilinear interpolation. The MSSIM, which accounts well for the texture changes introduced by the super-resolution process, has its values increased by the super-

resolution algorithm. Since this measure was created to better reflect perceived visual quality by humans [29][28], this implies that the super-resolution algorithm increases perceptual quality.

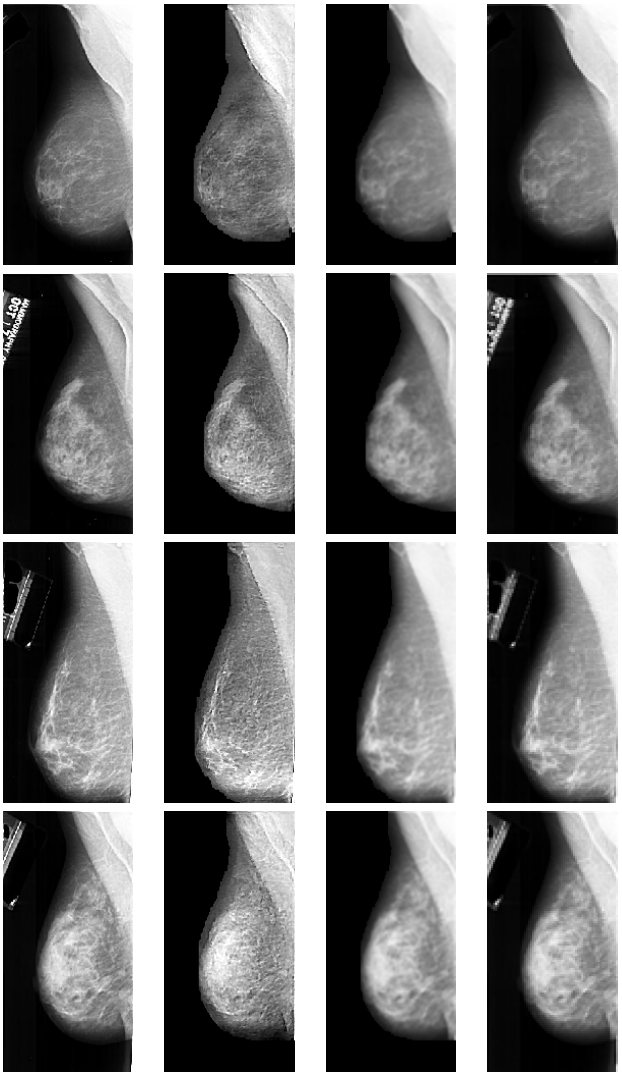

(a) (b) (c) (d)

Fig. 2. Sample super-resolution results with a downsample factor of 2: (a) Original high-resolution image. (b) Super-resolution image. (c) Interpolated image. (d) low-resolution image

V. Conclusions and Future Work

In this work, we presented a new way to improve the quality of X-ray images without having to use more radiation, which increases health risks of patients. The method takes low-resolution images obtained with low doses of X-ray radiation, and automatically registers and aligns them using mesh warping, and then uses super-resolution algorithms to create high resolution images from the LR input. Our results show that the super-resolution algorithm can generate accurate high-resolution breast mammograms from low-resolution input with no manual registration.

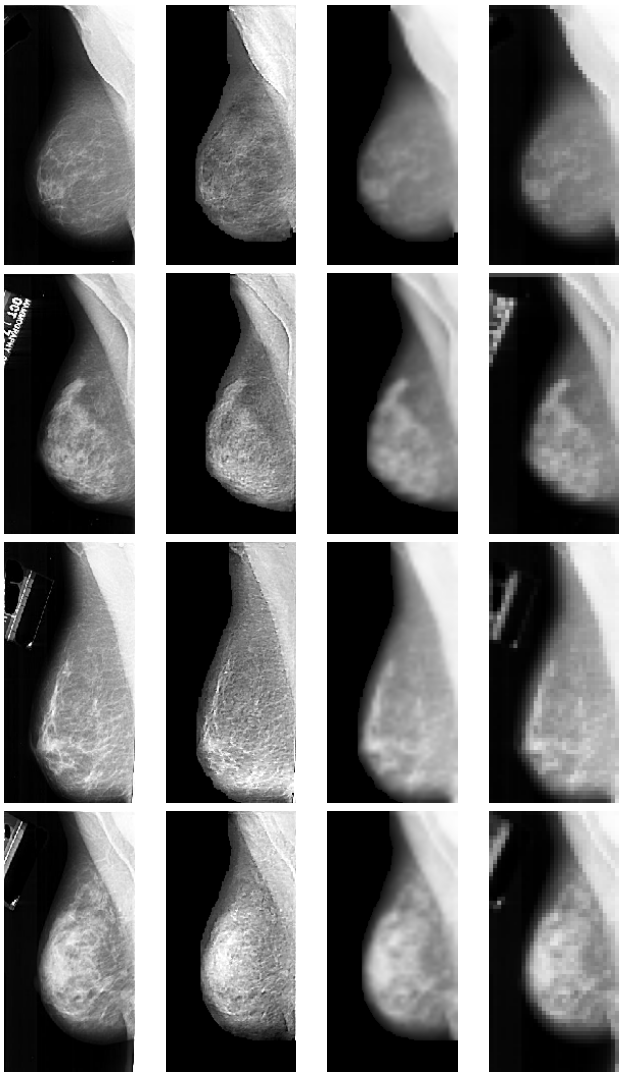

(a) (b) (c) (d)

Fig. 3. Sample super-resolution results with a downsample factor of 4: (a) Original high-resolution image. (b) Super-resolution image. (c) Interpolated image. (d) low-resolution image

As medical imaging moves towards complete digital imaging and produces prohibitively large amounts of data, compression is necessary for storage and communication purposes. Our method has the potential to eliminate the need to store images at full resolution, since they could be re-generated them from low-resolution ones. We will explore different trade-off between compression rates and accuracy, as well as analyze the interaction between our method and conventional compression schemes.

Though the SR images have very high-resolution, some details in the SR images are different from the original images. We will study whether these differences would affect diagnosis by applying an automatic breast cancer detection system to the original images and SR images respectively, and then compare the detection rates.

To further improve the speed of the super-resolution algorithm, we plan to use stream processing to parallelize the

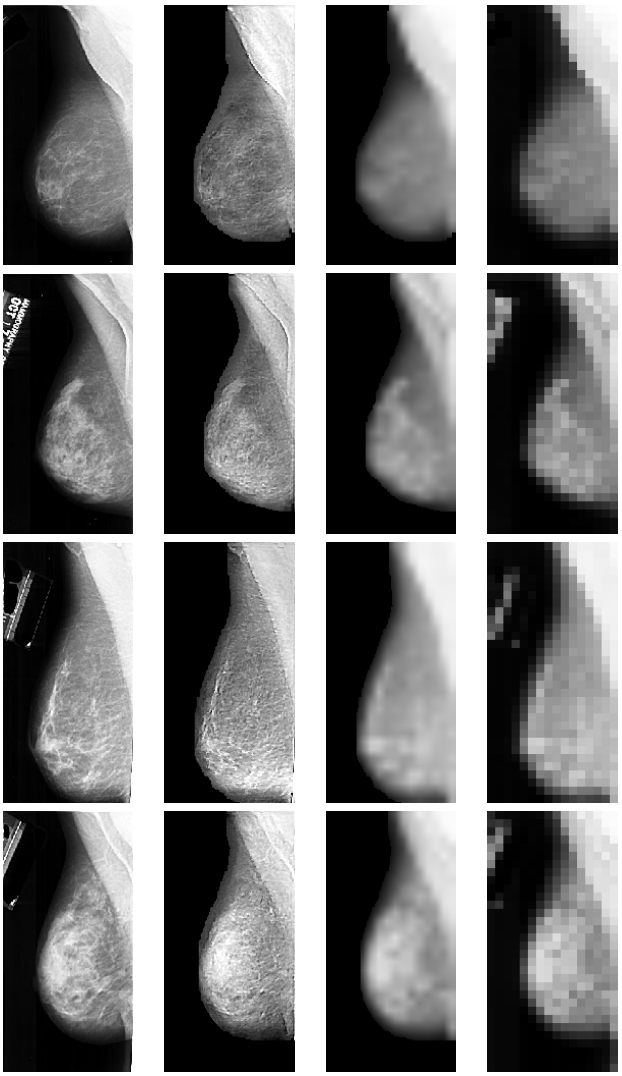

(a) (b) (c) (d)

Fig. 4. Sample super-resolution results with a downsample factor of 8: (a) Original high-resolution image. (b) Super-resolution image. (c) Interpolated image. (d) low-resolution image

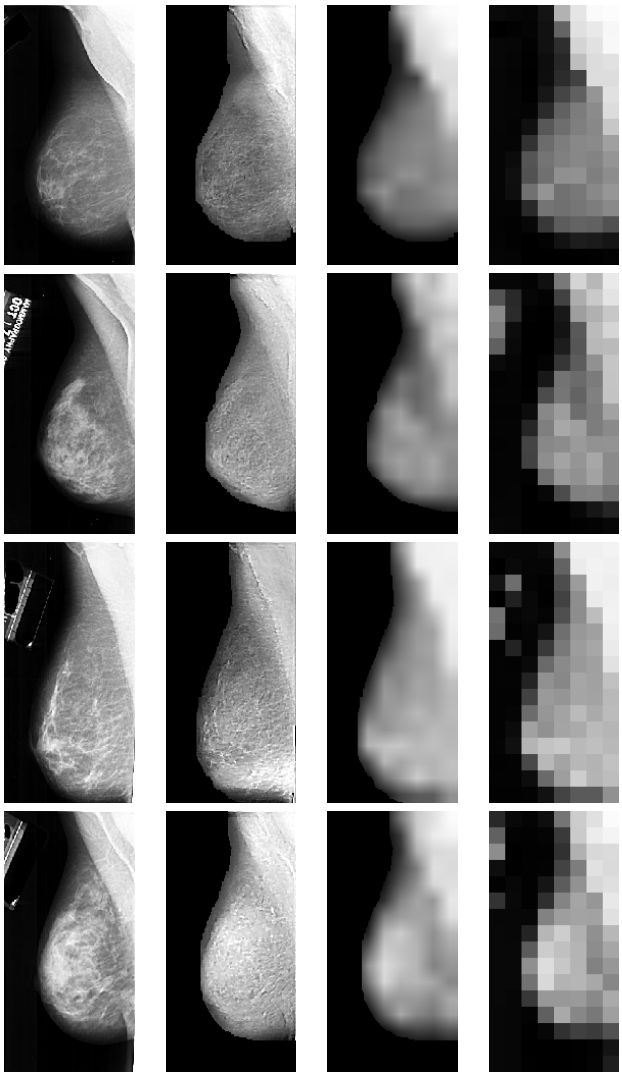

(a) (b) (c) (d)

Fig. 5. Sample super-resolution results with a downsample factor of 16: (a) Original high-resolution image. (b) Super-resolution image. (c) Interpolated image. (d) low-resolution image

execution. Stream processing permits the execution of data-parallel algorithms with stream processors such as graphic processing units (GPUs), while using the central processing unit (CPU) for other purposes simultaneously. This would enable a conventional PC to run the image super-resolution algorithm in real time.

REFERENCES

[1] A. Jemal, R. Siegel, E. Ward, Y. Hao, J. Xu, and M. J. Thun, "Cancer statistics," *CA Cancer J Clin*, vol. 59, no. 4, pp. 225–249, 2009.

[2] M. D. Robinson, S. Farsiu, J. Y. Lo, P. Milanfar, and C. A. Toth, "Efficient multiframe registration of aliased x-ray images," in *Proceedings of the 41th Asilomar Conference on Signals, Systems, and Computers*, Pacific Grove, CA, November 2007.

[3] M. Irani and S. Peleg, "Improving resolution by image registration," in *Proceedings of CVGIP: Graphical Models and Image Process*, vol. 53, no. 3, May 1991, pp. 231–239.

[4] H. Greenspan, G. Oz, N. Kiryati, and S. Peled, "Super-resolution in mri," in *Proceedings of IEEE International Symposium on Biomedical Imaging*, 2002, pp. 943–946.

[5] J. A. Kennedy, O. Israel, A. Frenkel, R. Bar-Shalom, and H. Azhari, "Super-resolution in pet imaging," *IEEE transactions on medical imaging*, vol. 25, no. 2, pp. 137–147, February 2006.

[6] ——, "Improved image fusion in pet/ct using hybrid image reconstruction and super-resolution," *International Journal of Biomedical Imaging*, 2007.

[7] A. Kanemura, S. Maeda, and S. Ishii, "Hyperparameter estimation in bayesian image superresolution with a compound markov random field prior," in *IEEE workshop on Machine Learning for Signal Processing*, August 2007, pp. 182–186.

[8] A. Wong and J. Scharcanski, "Phase-adaptive superresolution of mammographic images using complex wavelets," *IEEE transactions on image processing*, vol. 18, no. 5, pp. 1140–1146, May 2009.

[9] S. Baker and T. Kanade, "Limits on super-resolution and how to break them," *IEEE Transactions on Pattern Analysis and Machine Intelligence*, vol. 24, no. 9, pp. 1167–1183, 2002.

[10] X. Wang and X. Tang, "Face hallucination and recognition," in *Proceedings of the Fourth International Conference on Audio- and Video-Based Personal Authentication (IAPR)*, University of Surrey, Guildford, U.K., June 2003, pp. 486–494.

[11] S. C. Park, M. K. Park, and M. G. Kang, "Super-resolution image reconstruction: a technical overview," *Signal Processing Magazine,*

TABLE I
IMAGE QUALITY MEASURES

Method	Downsample factor	PSNR	MSSIM
Super-resolution	16	35.7403	0.8095
	8	34.7535	0.8238
	4	34.0200	0.8242
	2	33.4649	0.8223
Nearest-neighbor interpolation	16	31.5602	0.6164
	8	32.9498	0.6690
	4	34.4359	0.7600
	2	36.6833	0.8558
Bilinear interpolation	16	32.3788	0.7282
	8	33.9344	0.7577
	4	35.2363	0.8072
	2	37.1938	0.8807

IEEE, vol. 20, no. 3, pp. 21–36, May 2003.

[12] C. B. Atkins, C. A. Bouman, and J. P. Allebach, "Optimal image scaling using pixel classification," in *2001 International Conference on Image Processing. Volume*, 2001, pp. 864–867.

[13] N. Dodgson, "Quadratic interpolation for image resampling," *IEEE Transactions on Image Processing*, vol. 6, no. 9, pp. 1322–1326, September 1997.

[14] W. T. Freeman, E. C. Pasztor, and O. T. Carmichael, "Learning low-level vision," *International Journal on Compter Vision*, vol. 40, no. 1, pp. 25–47, 2000.

[15] H. Greenspan, C. Anderson, and S. Akber, "Image enhancement by nonlinear extrapolation in frequency space," *IEEE Transactions on Image Processing*, vol. 9, no. 6, pp. 1035–1048, June 2000.

[16] S. Baker and T. Kanade, "Hallucinating faces," in *Fourth IEEE International Conference on Automatic Face and Gesture Recognition*, Grenoble, France, March 2000.

[17] G. Dedeoğlu, "Exploiting space-time statistics of videos for face "hallucination"," Ph.D. dissertation, The Robotics Institute, Carnegie Mellon University, Pittsburgh, Pennsylvania, April 2007.

[18] W. T. Freeman, T. R. Jones, and E. C. Pasztor, "Example-based super-resolution," *IEEE Computer Graphics and Applications*, vol. 22, no. 2, pp. 56–65, 2002.

[19] L. Liang, C. Liu, Y. Xu, B. Guo, and H.-Y. Shum, "Real-time texture synthesis by patch-based sampling," *ACM Transactions on Graphics*, vol. 20, no. 3, pp. 127–150, July 2001.

[20] C. Liu, H.-Y. Shum, and W. T. Freeman, "Face hallucination: Theory and practice," *International Journal of Computer Vision (IJCV)*, vol. 75, no. 1, pp. 115–134, October 2007.

[21] C. Liu, H.-Y. Shum, and C.-S. Zhang, "A two-step approach to hallucinating faces: global parametric model and local nonparametric model," in *Proceedings of the 2001 IEEE Conference on Computer Vision and Pattern Recognition (CVPR 2001)*, 2001, pp. 192–198.

[22] X. Wang and X. Tang, "Hallucinating face by eigentransformation," *IEEE Transactions on Systems, Man and Cybernetics, Part C: Applications and Reviews*, vol. 35, no. 3, pp. 425–434, August 2005.

[23] J. T. Hsu1, C. C. Yen, C. C. Li, M. Sun, B. Tian, and M. Kaygusuz, "Application of wavelet-based pocs superresolution for cardiovascular mri image enhancement," in *Proceedings of the Third International Conference on Image and Graphics (ICIG04)*, 2004, pp. 572–575.

[24] A. H. Lettington and Q. H. Hong, "Ringing artifact reduction for poisson map superresolution algorithms," in *IEEE SIGNAL PROCESSING LETTERS*, vol. 2, no. 5, May 1995, pp. 83–84.

[25] M. Nguyen, P. Atkinson, and H. Lewis, "Superresolution mapping using a hopfield neural network with lidar data," *IEEE Geoscience and Remote Sensing Letters*, vol. 2, no. 3, pp. 366–370, July 2005.

[26] G. Wolberg, *Digital Image Warping*. IEEE Computer Society Press, 1990, ch. 2-Pass Mesh Warping, pp. 222–240.

[27] I. Bégin and F. P. Ferrie, "Comparison of super-resolution algorithms using image quality measures," in *Proceedings of the 3rd canadian conference on computer and robot vision*. Washington, DC, USA: IEEE Computer Society, 2006, p. 72.

[28] Z. Wang, A. C. Bovik, H. R. Sheikh, and E. P. Simoncelli, "Image quality assessment: From error visibility to structural similarity," *IEEE Transactions on Image Processing*, vol. 13, no. 4, pp. 600–612, April 2004.

[29] B. Girod, "What's wrong with mean-squared error?" in *Digital images and human vision*, MIT Press, Cambridge, MA. ISBN 0-262-23171-9, 1993, pp. 207–220.